# Dual absorber $Fe_2O_3$/$WO_3$ host-guest architectures for improved charge generation and transfer in photoelectrochemical applications

You may also be interested in:

# Materials Research Express

**PAPER**

# Dual absorber $Fe_2O_3$/$WO_3$ host-guest architectures for improved charge generation and transfer in photoelectrochemical applications

Alexander Müller[1,2,3,4], Ilina Kondofersky[2,4], Alena Folger[1], Dina Fattakhova-Rohlfing[2], Thomas Bein[2] and Christina Scheu[1]

1   Max-Planck-Institut für Eisenforschung GmbH (MPIE), Max-Planck-Strasse 1, 40237 Düsseldorf, Germany
2   Department of Chemistry and Center for NanoScience (CeNS), University of Munich (LMU), Butenandtstrasse 5-13, 81377 Munich, Germany
3   Present address: National Center for Electron Microscopy, Molecular Foundry, Lawrence Berkeley National Laboratory, 1 Cyclotron Rd, Berkeley, CA 94720, United States of America
4   These authors contributed equally.

E-mail: scheu@mpie.de

## Abstract

In this study the influence of the spatial distribution and of different nanostructures of $WO_3$ and $Fe_2O_3$ in the dual absorber system $Fe_2O_3$/$WO_3$ was systematically investigated for the first time. $WO_3$ was applied as a scaffold and/or as a surface treatment to mesoporous $Fe_2O_3$ films. Both approaches strongly increased the performance compared to the individual photoabsorbers. By combining a host guest architecture with a surface treatment, current densities of about $0.7\,mA\,cm^{-2}$ at 1.23 V versus reversible hydrogen electrode under AM 1.5 illumination with an incident photon-to-current efficiency of 17% at 350 nm were achieved without the use of further catalysts. We could identify several beneficial interactions between $Fe_2O_3$ and $WO_3$. $WO_3$ strongly scatters visible light, resulting in increased absorption by $Fe_2O_3$ and higher current densities. We also determined a cathodic shift in the onset potential to 0.8 V and increased transfer rates of up to 88%. This combination of beneficial effects proves the viability of the presented device architecture.

## 1. Introduction

Driven by climate change, rapid population growth and dwindling resources, research into alternative, sustainable energies is thriving. Solar cells and wind turbines, which harness the power of the sun, already play a major role in the energy mix of some countries, with their market share expected to increase. However, storage of the generated electricity is a challenge. One of many possible solutions is photoelectrochemical water splitting, which uses sun light as an energy source to generate oxygen and hydrogen from water. While suitable photoelectrode materials have been studied since 1972 [1], research has intensified in the last few years and several photocathode and photoanode materials (such as $TiO_2$, Si or $Cu_2O$ and $Fe_2O_3$, $WO_3$ or $BiVO_4$, respectively) have been investigated [2–4]. Efficient photoanodes, in particular, are difficult to realize. Producing one oxygen molecule requires four holes, making recombination likely and requiring significant optimization of factors such as composition, electronic structure and morphology. All efforts notwithstanding, it is becoming more and more obvious that limitations intrinsic to many single absorber materials investigated so far, such as large band gaps, slow surface kinetics or fast bulk electron–hole recombination, are difficult to overcome. One approach towards solving this problem is the combination of different photoabsorber materials. Such a combination can increase the efficiency in several ways such as by optical absorption enhancement, enhanced charge separation, faster surface kinetics, or the modification of the electronic structure of the interface between both materials [5]. For photoanodes, a dual absorber approach has been successful for several systems such as $WO_3$/$TiO_2$ [6], $WO_3$/$BiVO_4$ [7], $TiO_2$/$Fe_2O_3$ [8] and $Fe_2O_3$/$WO_3$ [5, 9, 10].

The $Fe_2O_3$/$WO_3$ system is a good model and a promising photoanode for many reasons. The individual materials are abundant and therefore cheap, non-toxic and corrosion-resistant [11, 12]. Consequently, both materials have been intensively studied, and the influence of different morphologies, dopants, surface modifications etc for both systems is well-investigated [11, 13]. $WO_3$ has a band gap of 2.5–2.8 eV and absorbs mostly in the blue and UV spectral range [12, 14, 15]. Because of good charge transport properties and fast surface kinetics, it has proven itself a suitable candidate for water photoelectrolysis [15]. However, the large band gap limits the overall theoretical solar-to-hydrogen efficiency to 8% [16]. $Fe_2O_3$, on the other hand, has a band gap between 1.9 and 2.2 eV and also absorbs a large fraction of visible light, driving the potential solar-to-hydrogen efficiency up to 16.8% [11, 16]. Unfortunately, the expected efficiency is greatly reduced by several loss mechanisms such as high bulk and surface recombination rates and slow kinetics for the oxygen evolution reaction. Combining $Fe_2O_3$ and $WO_3$ can improve the performance of the individual materials in several ways. Compared to bare $WO_3$, a larger spectral range is absorbed. The band alignment of $Fe_2O_3$ and $WO_3$ allows for the injection of electrons from $Fe_2O_3$ into $WO_3$, with the latter being a better electron conductor. Holes, on the other hand, are injected from $WO_3$ into $Fe_2O_3$ [17]. Sivula *et al* found the deposition of $Fe_2O_3$ onto $WO_3$ scaffolds to drastically improve electron charge collection [9]. Furthermore, the rate of the oxygen evolution reaction of $Fe_2O_3$ was shown to be significantly improved by surface treatment of $Fe_2O_3$ by a $WO_3$ layer [5, 18].

In addition to the strategies discussed above, nanostructuring is commonly employed to improve photoelectrodes [19, 20]. Several morphologies have so far been synthesized in the $Fe_2O_3$/$WO_3$ system, including flat and porous films [21–26], host-guest architectures [9], and nanowires [5, 10, 27]. Here, we for the first time systematically investigated the influence of the spatial distribution and the nanostructuring approach. $WO_3$ was applied both as a scaffold and as a surface treatment, allowing correlation between morphology and performance. Mesoporous Sn-doped $Fe_2O_3$ photoabsorber layers were prepared by a sol-gel approach and deposited onto a continuous, macroporous $WO_3$ scaffold [28]. We chose Sn-doped $Fe_2O_3$ following prior work in which we had shown that Sn increases the transfer efficiency and thereby the photocurrent. In the following, we are referring to Sn-doped $Fe_2O_3$ whenever we use the expression '$Fe_2O_3$' to describe a sample or a component of one. The performance was increased even further by depositing a $WO_3$ surface layer and increasing the $Fe_2O_3$/$WO_3$ interfacial area, thus reaching photocurrents of up to 0.7 mA cm$^{-2}$ at 1.23 V versus the reversible hydrogen electrode (RHE). The viability of this host-guest approach was confirmed by comparing the macroporous photoanodes to mesoporous reference samples [9, 10, 29–33]. As $WO_3$ only absorbs a small fraction of blue light, whereas hematite strongly absorbs in this region, measuring photocurrent transients under UV and under blue light illumination allowed for a more nuanced discussion of the impact of the morphology on the photoelectrochemical performance and gave further insights into a complex interplay of several effects such as transfer rate enhancement or increased light absorption.

## 2. Materials and methods

### 2.1. Preparation of $WO_3$ films
The precursor solution for $WO_3$ was prepared by adding 0.8 g of $(NH_4)_6H_2W_{12}O_{40} \cdot xH_2O$ to 3 ml of deionized water (Millipore Q). To create flat layers, this solution was dip-coated onto the fluorine doped tin oxide (FTO) substrate under ambient conditions at a rate of 38 mm min$^{-1}$. The samples were subsequently calcined at 500 °C with a ramp of 3 °C min$^{-1}$ and a dwell time of 5 h. By applying the same procedure to polymethylmethacrylate (PMMA, synthesized according to a well-established procedure [29, 34, 35]) or hematite films, macroporous inverse opal scaffolds and overlayers, respectively, could be prepared.

### 2.2. Synthesis and deposition of tin-doped hematite
A procedure developed by Dunn *et al* [28] was applied for the synthesis of tin-doped hematite. 0.25 g Pluronic® P123 were dissolved in 10 ml *tert*-butanol under vigorous stirring. 0.1106 g (0.3 mmol) $Sn(CH_3COO)_4$ were added to the solution and stirred for 5 h. Next, $Fe(NO_3)_3 \cdot 9H_2O$ (0.505 g, 1.25 mmol) was added at room temperature and sonicated for 15 min. 2.5 ml water were then added and the solution was left to stir for 17 h under ambient conditions. Prior to spin coating, the resulting suspension was filtered through a filter with a pore diameter of 200 nm. The electrodes were prepared by depositing the filtered solution (100 $\mu$l) onto FTO or the macroporous scaffold, respectively, by spin coating at 1000 rpm for 30 s. The films were then calcined at 600 °C with a ramp of 3 °C min$^{-1}$ and a dwell time of 30 min.

### 2.3. Crystallographic, structural and chemical analysis
Powder x-ray diffraction (XRD) patterns were acquired on a STOE powder diffractometer (Cu-K$\alpha$1, $\lambda = 1.5406$ Å) equipped with a position-sensitive Mython-1K detector in transmission geometry.

Scanning electron microscopy (SEM) measurements were performed on a Zeiss Auriga scanning electron microscope with a field emission gun operated at 4 kV and equipped with an EDAX solid state energy-dispersive x-ray (EDX) spectroscopy detector.

Morphology, crystallography and elemental distribution were investigated using a probe-corrected FEI Titan Themis transmission electron microscope (TEM) with a high brightness field emission gun operating at 300 kV. Scanning TEM (STEM) images were acquired with an annular dark-field (ADF) detector and the distribution of $Fe_2O_3$ and $WO_3$ was mapped by collecting EDX spectra in STEM with four Super-X Bruker solid state detectors. Samples in cross-sectional geometry were prepared following a procedure developed by Strecker *et al* [36].

### 2.4. Optical characterization

UV–Vis spectra were measured under illumination through the substrate on a Perkin Elmer Lambda 1050 UV/Visible/NIR spectrophotometer with an integrating sphere. The absorbance of the films was calculated by measuring both transmittance and reflectance and correcting for the absorbance of the FTO substrate using an expression derived by Klahr *et al* [37].

### 2.5. Photoelectrochemical characterization

Current–voltage (CV) and incident photon-to-current efficiency (IPCE) curves were measured with a $\mu$-Autolab III potentiostat with a FRA2 impedance analyzer. All but an area of $0.2\,cm^2$ was masked with a Teflon-coated glass fiber adhesive tape. The sample was placed into a quartz cell filled with an aqueous 0.1 M NaOH electrolyte and connected, with an Ag/AgCl reference electrode and a Pt mesh counter electrode, to the potentiostat. To obtain CV curves, the films were illuminated through the substrate by an AM 1.5 solar simulator (Solar Light Model 16S) at $100\,mW\,cm^{-2}$ by scanning from negative to positive potentials in the dark or under illumination at a sweep rate of $20\,mV\,s^{-1}$.

IPCE measurements were performed under monochromatic light chopped with a frequency of 1 Hz. Samples were illuminated through the substrate by a 150 W Xenon lamp equipped with a monochromator and order-sorting filters. All IPCE values were measured at a sample bias of 1.23 V versus RHE under simulated solar irradiation. The light intensity at the electrode was determined using a certified, KG5-filtered Fraunhofer ISE silicon reference cell.

Photocurrent transient data were acquired with a 365 nm or a 455 nm light-emitting diode and a chopping frequency of 2 Hz at an applied potential of 1.23 V versus RHE. The light intensities were calibrated with a Fraunhofer ISE silicon certified photovoltaic cell and correspond to 3.2 mA ($160\,W\,m^{-2}$). Transfer efficiencies were calculated as the ratio of the steady-state and the initial photocurrent density. As transfer efficiencies measured with 365 nm light did not deviate by more than $\pm2\%$ from those measured with 455 nm light and are effectively independent of the illumination wavelength, the transfer efficiencies averaged over both wavelengths will be discussed.

## 3. Results and discussion

Two series of samples were prepared by sol-gel synthesis (figure 1).

The first series of flat layers served as references to the host-guest electrodes and allowed analyzing performance-enhancing factors on simple model systems. This series comprised three samples, including a compact $WO_3$ and a mesoporous $Fe_2O_3$:Sn layer coated onto FTO as well as a dual absorber photoelectrode prepared by depositing a $WO_3$ overlayer onto a $Fe_2O_3$:Sn film. These samples are labeled '$WO_3$', '$Fe_2O_3$' and '$Fe_2O_3/WO_3$', respectively. The second series demonstrated the performance-enhancing benefits of the host-guest architecture. A macroporous $WO_3$ scaffold was infiltrated by $Fe_2O_3$:Sn and coated with an additional $WO_3$ overlayer. In the remainder of the text, these samples are labeled '$mWO_3$', '$mWO_3/Fe_2O_3$', and '$mWO_3/Fe_2O_3/WO_3$', respectively. It should be noted that $WO_3$ is known to potentially fulfill several functions. At wavelengths below the optical absorption limit, $WO_3$ acts as a photoabsorber. Due to its favorable band alignment, it can also act as a majority charge carrier collector of electrons generated in $Fe_2O_3$ [9]. Finally, $WO_3$ can act as a surface treatment to $Fe_2O_3$ photoanodes, suppressing electron–hole recombination on the surface [5]. The samples in this study were prepared so that all three possible performance-enhancing effects could be studied systematically.

XRD patterns confirmed the successful synthesis of phase-pure $Fe_2O_3$:Sn in the hematite structure and of monoclinic $WO_3$ (figure SI 1) (stacks.iop.org/MRX/4/016409/mmedia) [38, 39]. Other phases or reaction products could not be detected by XRD, SEM or TEM. In accordance with previous work by Dunn *et al*, cross-sectional analysis of mesoporous $Fe_2O_3$ layers showed ~50 nm thick mesoporous films composed of individual nanoparticles with an average size of ~40 nm × 80 nm (figures 2(b) and (c)) [28]. $WO_3$, in contrast, forms ~100 nm thick, cracked layers composed of large, compact platelets between a few hundred nanometers and a few micrometers in size (figure SI 2). The $Fe_2O_3/WO_3$ dual absorber retains these morphologies, with $WO_3$ both infiltrating the $Fe_2O_3$ layer, with an accumulation at the FTO, and forming a ~50 nm thick layer on top (figures 2(a), (c) and (d)). By forming a compact top layer, $WO_3$ decreases the exposed $Fe_2O_3$ surface area.

In contrast, the macroporous samples have an open, porous morphology (figure 2(d)). The macroporous $WO_3$ scaffold forms a ~2.5 $\mu$m thick layer with ~150 nm wide pores (figure 2(g)). Even though the scaffold is distorted compared to a perfect inverse opal structure, it is continuous and reaches the back contact. This should
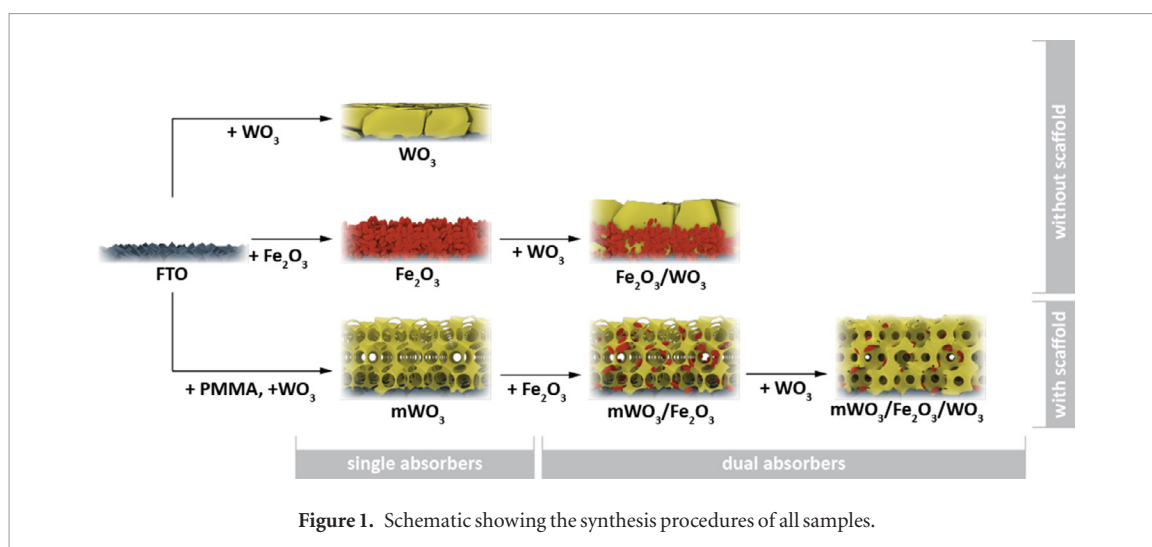
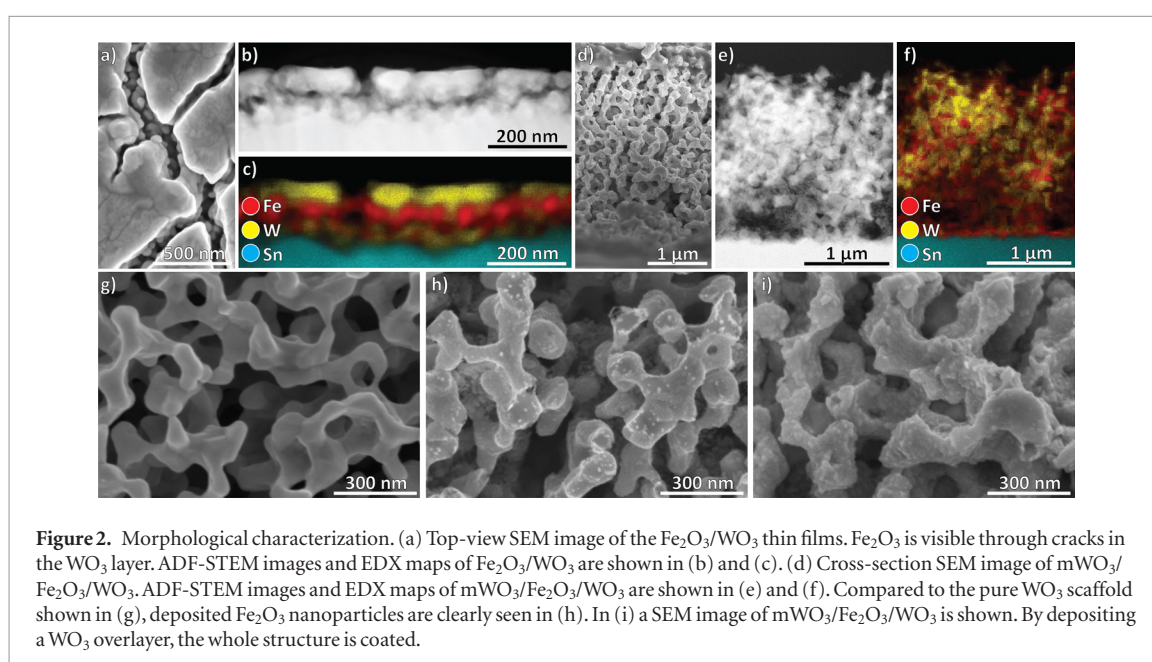**Figure 1.** Schematic showing the synthesis procedures of all samples.



**Figure 2.** Morphological characterization. (a) Top-view SEM image of the $Fe_2O_3/WO_3$ thin films. $Fe_2O_3$ is visible through cracks in the $WO_3$ layer. ADF-STEM images and EDX maps of $Fe_2O_3/WO_3$ are shown in (b) and (c). (d) Cross-section SEM image of $mWO_3/Fe_2O_3/WO_3$. ADF-STEM images and EDX maps of $mWO_3/Fe_2O_3/WO_3$ are shown in (e) and (f). Compared to the pure $WO_3$ scaffold shown in (g), deposited $Fe_2O_3$ nanoparticles are clearly seen in (h). In (i) a SEM image of $mWO_3/Fe_2O_3/WO_3$ is shown. By depositing a $WO_3$ overlayer, the whole structure is coated.

be beneficial for charge transport. Hematite nanoparticles fully infiltrate the scaffold and are homogenously distributed throughout the whole film (figures 2(e) and (f)). An additional thin layer of $Fe_2O_3$ nanoparticles forms on the FTO substrate (figure 2(f)). In contrast to the flat layers, a $WO_3$ overlayer fully infiltrates the scaffold and thinly coats $WO_3$ scaffold and $Fe_2O_3$ nanoparticles alike without top layer formation (figure 2(i)).

The crystal structures of the materials were investigated by TEM. Monocrystallinity of hematite nanoparticles prepared by this synthesis procedure has previously been shown by Dunn *et al* [28]. Both the $WO_3$ scaffold and the $WO_3$ overlayer are highly crystalline, with $mWO_3$ having domains of several hundred nanometers in size (figures 3(a) and (b)). In both $Fe_2O_3/WO_3$ and $mWO_3/Fe_2O_3$, an abrupt interface between $Fe_2O_3$ and $WO_3$ without specific orientation relationships or amorphous phases was found (figure 3(c)).

Light absorption of all samples was assessed with UV–Vis measurements (figure 4). Like the photoelectrochemical measurements, they were done under substrate illumination.

As expected from the band gap, bare $WO_3$ only absorbs light up to a wavelength of ~425 nm. In comparison, $Fe_2O_3$ absorbs light up to a wavelength of ~560 nm, consistent with a band gap of 2.2 eV, and thereby a much larger percentage of the solar spectrum. Of the flat layers, $Fe_2O_3$ absorbs more light than $WO_3$ throughout the whole spectral range. In both flat and macroporous samples, more light is absorbed upon deposition of a mesoporous $Fe_2O_3$:Sn layer or a $WO_3$ overlayer. Notable is the strong scattering contribution of both compact and macroporous $WO_3$, which is reduced for all *dual* absorbers (figures 4(c) and (f)). As the UV–Vis spectra were acquired under substrate illumination, light must be backscattered by $WO_3$ and absorbed by the $Fe_2O_3$ layer. $WO_3$ acting as a reflective layer in the visible range (figures 4(c) and (f)) significantly increases the absorbance (figure 4(b) and (e)). Unfortunately, this increase in absorbance is not expected to contribute to the photocurrent, as it is above the absorption cut-off of both $Fe_2O_3$ and $WO_3$. However, future studies, in which an additional photoabsorber is introduced, might benefit from this increase in scattering.
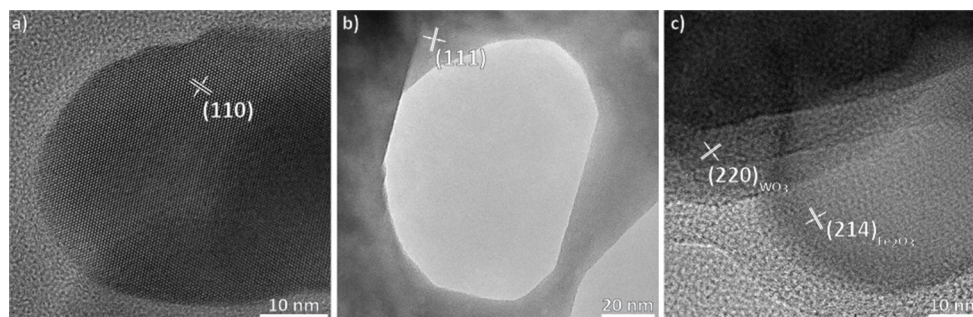
**Figure 3.** HRTEM images of (a) the WO₃ overlayer in Fe₂O₃/WO₃ and (b) the WO₃ scaffold. (c) Interface between Fe₂O₃ and WO₃.
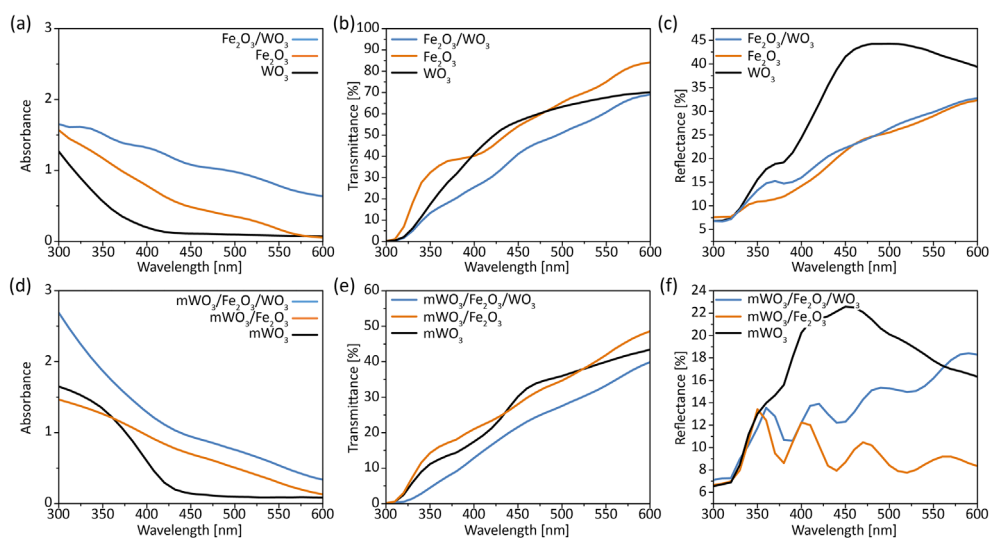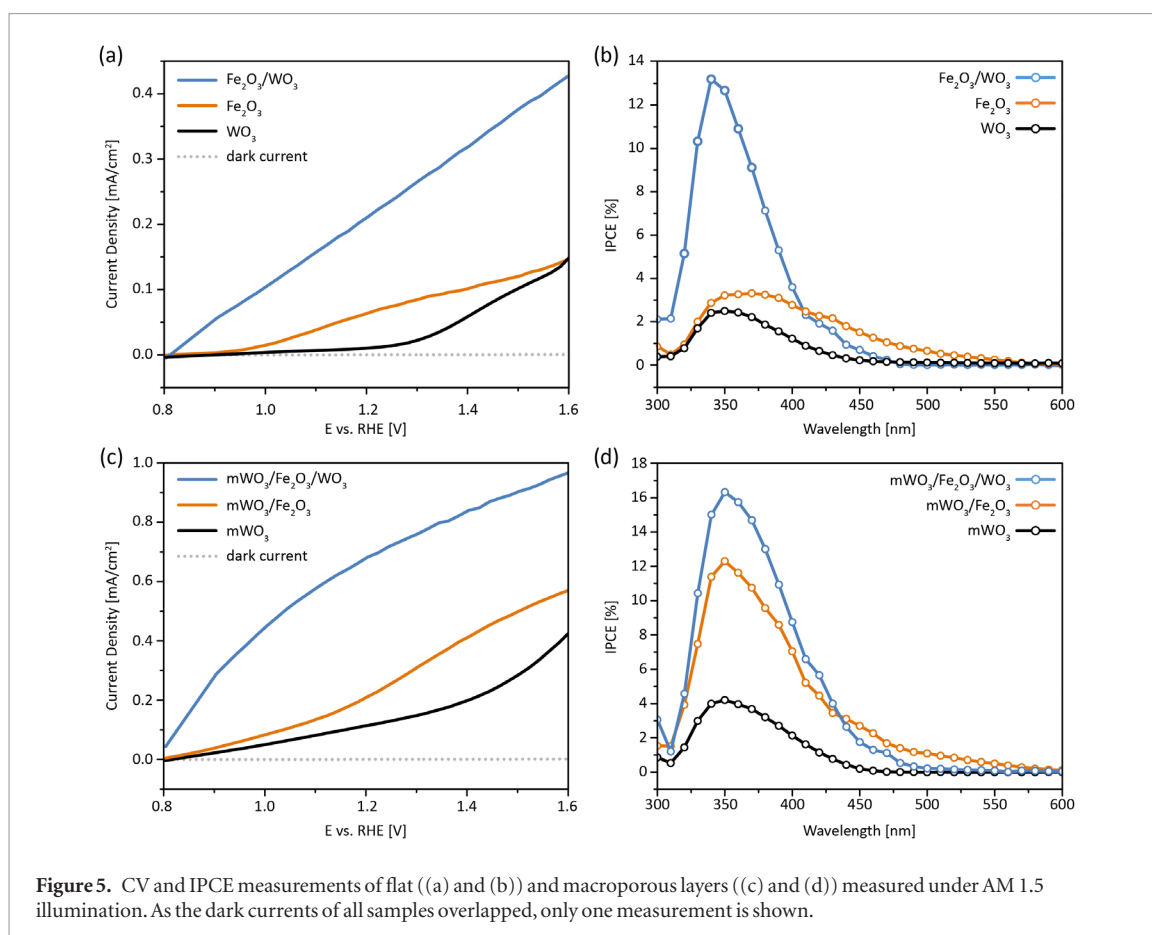


**Figure 4.** UV–Vis, transmittance and reflectance spectra of mesoporous ((a)–(c)) and macroporous ((d)–(f)) samples.

All samples were photoelectrochemically characterized by CV measurements under AM 1.5 illumination and by IPCE measurements (figure 5). Among the flat layers, Fe₂O₃ has a higher current density than WO₃ (0.01 mA cm⁻² at 1.23 V versus RHE compared to 0.08 mA cm⁻² at 1.23 V versus RHE), which can be explained by increased light harvesting in the visible region. In accordance with the drop in light absorbance seen in the UV–Vis spectra, the IPCE spectrum of bare WO₃ drops to 0% at ~425 nm, whereas the IPCE spectrum of Fe₂O₃ drops to 0% at a much longer wavelength of ~560 nm. Depositing a WO₃ layer onto Fe₂O₃, thus creating a dual absorber, increases the current density threefold compared to Fe₂O₃ and 17-fold compared to WO₃, with currents of 0.23 mA cm⁻² at 1.23 V versus RHE and a maximum IPCE of up to 13% at 340 nm. This dual absorber not only outperforms the single components, but also the sum of current densities obtained from the individual absorber layers, suggesting that the increased performance cannot be explained solely by increased light absorption. Another important feature of the dual absorber photoanodes is a cathodic shift of the onset potential by nearly 200 mV. Such a shift is usually attributed to the reduction of loss pathways due to either charge transfer catalysis or suppression of surface recombination [40–42].

The macroporous films show trends similar to the flat layer model systems (figure 5). The performance of the macroporous WO₃ scaffolds (0.13 mA cm⁻² at 1.23 V versus RHE) is strongly increased compared to WO₃ flat layers. As shown by UV/Vis measurements, the deposition of Fe₂O₃ leads to increased light absorption in the visible range and a shift of the IPCE curve, increasing the current density up to 0.24 mA cm⁻² at 1.23 V versus RHE. A substantial performance increase to 0.7 mA cm⁻² at 1.23 V versus RHE with a maximum IPCE of 17% at 350 nm is achieved by depositing an additional WO₃ layer. As for Fe₂O₃/WO₃, CV measurements of mWO₃/Fe₂O₃/WO₃ show a steep current onset at 0.8 V versus RHE. mWO₃/Fe₂O₃, which is also composed of both materials, does not show such a steep onset. The strong performance increases compared to flat layers could be explained by the increase in porosity and therefore surface area, or by the WO₃ scaffold acting as a current collector as described in the literature [9, 29]. Of note is the strong performance rise when applying WO₃ as a surface layer compared to having it as a scaffold. Interface-related effects such as suppressed recombination due to the WO₃ surface layer could therefore play a major role. Another possible explanation is the role of WO₃ as a scattering layer, which would increase the light harvesting efficiency of Fe₂O₃.

**Figure 5.** CV and IPCE measurements of flat ((a) and (b)) and macroporous layers ((c) and (d)) measured under AM 1.5 illumination. As the dark currents of all samples overlapped, only one measurement is shown.

The photocurrents discussed so far were measured under AM 1.5 illumination. However, given the band structures of $Fe_2O_3$ and $WO_3$ and based on our UV/Vis measurements, different processes are expected to take place under illumination with UV and with visible light (figure SI 3) [17]. Under UV illumination, electrons generated in $Fe_2O_3$ can be injected into $WO_3$ and holes generated in $WO_3$ can be injected into $Fe_2O_3$ (figure 6(a)), with the $WO_3$ scaffold expected to reduce recombination by efficient charge transport to the FTO substrate. Light of a longer wavelength, however, only generates electron–hole pairs in $Fe_2O_3$, of which the electrons can, according to the band diagram, be injected into $WO_3$ (figure SI 3). To gain further insight into the behavior of the dual absorber system, photocurrent transients were measured under chopped illumination with UV (365 nm) and blue (455 nm) light. Due to increased light absorption by both $Fe_2O_3$ and $WO_3$ in the UV region, steady-state photocurrents acquired under UV illumination are consistently higher than those measured with blue light (figure 6(b)). $WO_3$ is a highly efficient photocatalyst, leading to higher photocurrents than $Fe_2O_3$ under UV illumination [15]. Blue light, however, is not absorbed by $WO_3$ (figure 4) and $Fe_2O_3$ reaches higher photocurrents.

Photocurrent transients reflect all processes influencing charge transfer and transport in the electrode (figure 6) [28, 43]. Upon illumination, movement of photo-generated holes to the surface leads to a charging or displacement current. If holes accumulate, either due to slow surface kinetics or due to slow electron transport to the back contact, they recombine with electrons, and the initial photocurrent decays to a lower steady-state photocurrent. For $Fe_2O_3$, this leads to a characteristic 'spike and overshoot' photocurrent, whereas fast surface kinetics and good electron conductivity of pure $WO_3$ lead to a rectangular transient form suggestive of complete charge carrier extraction [43]. By depositing $Fe_2O_3$ onto a $WO_3$ scaffold, the difference between initial and steady-state photocurrent decreases compared to $Fe_2O_3$ and deposition of an additional $WO_3$ layer brings the shape of the photocurrent transient even closer to a rectangle. As expected from the fast surface kinetics and good charge transport properties the material is known for, both $WO_3$ and $mWO_3$ have transfer efficiencies of 100% [15]. In comparison and in accordance with previous work by Dunn *et al*, Sn-doped $Fe_2O_3$ has a transfer efficiency of 41% [28]. The transfer efficiency can be improved to 75% by depositing the Sn-doped $Fe_2O_3$ layer onto a $WO_3$ scaffold. In line with discussion in the literature, the $WO_3$ scaffold could act as a charge collector and thereby increase the electron diffusion length [9, 29]. In comparison, surface treatment by the deposition of an additional $WO_3$ layer has a greater effect on the transfer efficiency than the introduction of a $WO_3$ scaffold and increases the transfer efficiency to 85 and 88% for flat $Fe_2O_3/WO_3$ and macroporous $mWO_3/Fe_2O_3/WO_3$, respectively. The improved performance might stem from an enhanced rate of Faradaic reactions on the interface due to the surface treatment with $WO_3$. For both illumination wavelengths, photocurrent densities reached by the dual absorbers, regardless of whether $WO_3$
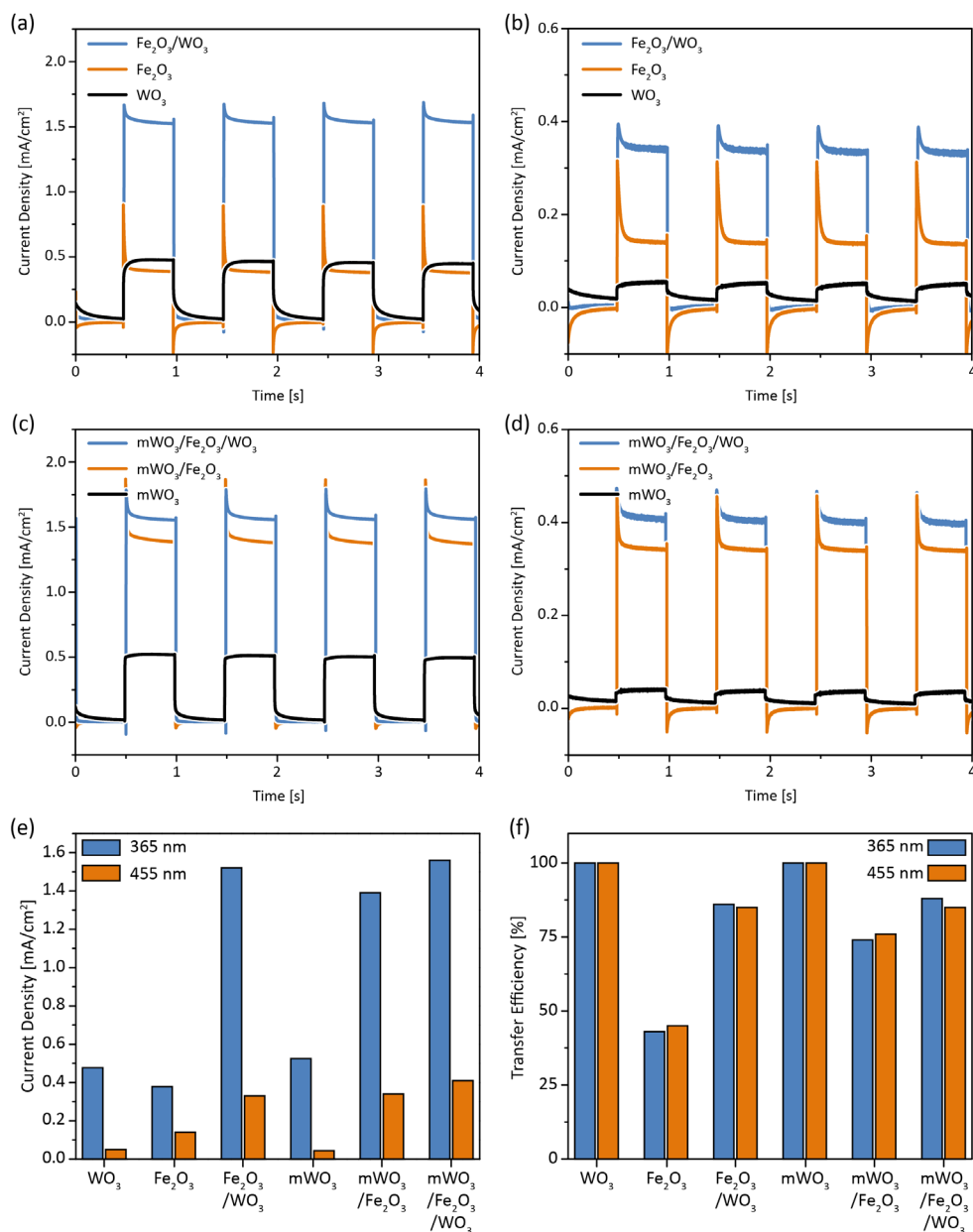
**Figure 6.** Photocurrent transients of flat layers under (a) UV (365 nm) and (b) blue (455 nm) illumination at an applied potential of 1.23 V versus RHE. Photocurrent transients of the macroporous layers under 365 nm and 455 nm illumination are shown in (c) and (d), respectively. (e) Steady-state photocurrent densities under illumination with 365 nm and 455 nm light at a potential of 1.23 V versus RHE. (f) Transfer efficiencies under illumination with 365 nm and 455 nm light extracted from photocurrent transients measured at 1.23 V ca. RHE.

was applied as a surface layer or as a scaffold, are very similar. This is in contrast to measurements under the full AM 1.5 solar spectrum, where a much larger difference in photocurrent densities was observed for the different architectures. This can presumably be explained by a complex interplay of several factors, such as faster surface kinetics, improved current collection and enhanced light absorption, in which $WO_3$ beneficially influences $Fe_2O_3$.

## 4. Conclusions

To systematically analyze the effects of $WO_3$ on $Fe_2O_3$ for photoelectrochemical water splitting, dual absorbers were prepared with $WO_3$ as a scaffold and/or as a surface layer. Both approaches significantly increased the performance, validating both the host-guest and the surface layer approach. By combining them, current densities of 0.7 mA cm$^{-2}$ at 1.23 V versus RHE under AM 1.5 illumination with an IPCE of 17% at 350 nm were reached. The performance increase was investigated by CV, IPCE, photocurrent transient and UV–Vis measurements and we could identify several beneficial effects responsible for improved charge carrier generation and transport. $WO_3$ strongly reflects visible light which in the dual absorbers is then absorbed by $Fe_2O_3$, resulting in increased light harvesting and thus higher photocurrents. Compared to $Fe_2O_3$, a cathodic shift of the onset potential from 1.0 to

0.8 V and an increase in transfer efficiencies, reaching up to 88%, were measured. We conclude that the investigated device architecture is a promising approach for the design of $Fe_2O_3$/$WO_3$ dual absorber photoanodes by combining different beneficial effects of different materials to produce substantially improved devices.

## Acknowledgments

## References

[1] Fujishima A and Honda K 1972 Electrochemical photolysis of water at a semiconductor electrode *Nature* **238** 37–8
[2] Grätzel M 2001 Photoelectrochemical cells *Nature* **414** 338–44
[3] Hisatomi T, Kubota J and Domen K 2014 Recent advances in semiconductors for photocatalytic and photoelectrochemical water splitting *Chem. Soc. Rev.* **43** 7520–35
[4] Li Z, Luo W, Zhang M, Feng J and Zou Z 2013 Photoelectrochemical cells for solar hydrogen production: current state of promising photoelectrodes, methods to improve their properties, and outlook *Energy Environ. Sci.* **6** 347–70
[5] Kronawitter C X, Vayssieres L, Shen S, Guo L, Wheeler D A, Zhang J Z, Antoun B R and Mao S S 2011 A perspective on solar-driven water splitting with all-oxide hetero-nanostructures *Energy Environ. Sci.* **4** 3889
[6] Wang J, Han Y, Feng M, Chen J, Li X and Zhang S 2011 Preparation and photoelectrochemical characterization of $WO_3$/$TiO_2$ nanotube array electrode *J. Mater. Sci.* **46** 416–21
[7] Su J, Guo L, Bao N and Grimes C A 2011 Nanostructured $WO_3$/$BiVO_4$ heterojunction films for efficient photoelectrochemical water splitting *Nano Lett.* **11** 1928–33
[8] Luan P, Xie M, Liu D, Fu X and Jing L 2014 Effective charge separation in the rutile $TiO_2$ nanorod-coupled $\alpha$-$Fe_2O_3$ with exceptionally high visible activities *Sci. Rep.* **4** 6180–6
[9] Sivula K, Formal F Le and Grätzel M 2009 $WO_3$–$Fe_2O_3$ photoanodes for water splitting: a host scaffold, guest absorber approach *Chem. Mater.* **21** 2862–7
[10] Jin T, Diao P, Wu Q, Xu D, Hu D, Xie Y and Zhang M 2014 $WO_3$ nanoneedles/a-$Fe_2O_3$/cobalt phosphate composite photoanode for efficient photoelectrochemical water splitting *Appl. Catal.* B **148–9** 304–10
[11] Sivula K, Le Formal F and Grätzel M 2011 Solar water splitting: progress using hematite ($\alpha$-$Fe_2O_3$) photoelectrodes *ChemSusChem* **4** 432–49
[12] Hodes G, Cahen D and Manassen J 1976 Tungsten trioxide as a photoanode for a photoelectrochemical cell (PEC) *Nature* **260** 312–3
[13] Liu X, Wang F and Wang Q 2012 Nanostructure-based $WO_3$ photoanodes for photoelectrochemical water splitting *Phys. Chem. Chem. Phys.* **14** 7894
[14] Granqvist C G 2000 Electrochromic tungsten oxide films: review of progress 1993–1998 *Sol. Energy Mater. Sol. Cells* **60** 201–62
[15] Santato C, Ulmann M and Augustyński J 2001 Photoelectrochemical properties of nanostructured tungsten trioxide films *J. Phys. Chem.* B **105** 936–40
[16] Murphy A B, Barnes P R F, Randeniya L K, Plumb I C, Grey I E, Horne M D and Glasscock J A 2006 Efficiency of solar water splitting using semiconductor electrodes *Int. J. Hydrog. Energy* **31** 1999–2017
[17] van de Krol R, Liang Y and Schoonman J 2008 Solar hydrogen production with nanostructured metal oxides *J. Mater. Chem.* **18** 2311
[18] Kishi T and Aritsuka M 1988 Photo-anodic behaviour of $\alpha$-ferric oxide film electrodes coated with various metal oxides *Surf. Coat. Technol.* **34** 345–53
[19] Osterloh F E 2013 Inorganic nanostructures for photoelectrochemical and photocatalytic water splitting *Chem. Soc. Rev.* **42** 2294–320
[20] Zhang P, Gao L, Song X and Sun J 2015 Micro- and nanostructures of photoelectrodes for solar-driven water splitting *Adv. Mater.* **27** 562–8
[21] Luo W, Yu T, Wang Y, Li Z, Ye J and Zou Z 2007 Enhanced photocurrent–voltage characteristics of $WO_3$/$Fe_2O_3$ nano-electrodes *J. Phys. D: Appl. Phys.* **40** 1091–6
[22] Memar A, Daud W R W, Hosseini S, Eftekhari E and Minggu L J 2010 Study on photocurrent of bilayers photoanodes using different combination of $WO_3$ and $Fe_2O_3$ *Sol. Energy* **84** 1538–44
[23] Hosseini S, Eftekhari E, Masoudi Soltani S, Memar A, Eghbali Babadi F, Dastorian Jamnani B, Ismail M H S and Jeffery Minggu L 2013 Effect of intermediate layer in photocurrent improvement of three-layer photoanodes using $WO_3$ and $Fe_2O_3$ *J. Environ. Chem. Eng.* **1** 1309–14
[24] Hosseini S, Eftekhari E, Masoudi Soltani S, Babadi F E, Minggu L J and Ismail M H S 2014 Synthesis, characterization and performance evaluation of three-layered photoanodes by introducing a blend of $WO_3$ and $Fe_2O_3$ for dye degradation *Appl. Surf. Sci.* **289** 53–61
[25] Mao A, Kim J K, Shin K, Wang D H, Yoo P J, Han G Y and Park J H 2012 Hematite modified tungsten trioxide nanoparticle photoanode for solar water oxidation *J. Power Sources* **210** 32–7
[26] Miecznikowski K, Ramírez A, Fiechter S, Bogdanoff P, Szaniawska E, Wadas A and Kulesza P J 2015 Development of hybrid tungsten oxide photoanodes admixed with borododecatungstate-polyanion modified-hematite: enhancement of water oxidation upon irradiation with visible light *Electrochim. Acta* **179** 379–85
[27] Li Y, Feng J, Li H, Wei X and Wang R 2016 Photoelectrochemical splitting of natural seawater with a-$Fe_2O_3$/$WO_3$ nanorod arrays *Int. J. Hydrog. Energy* **41** 4096–105
[28] Dunn H K, Feckl J M, Müller A, Fattakhova-Rohlfing D, Morehead S G, Roos J, Peter L M P, Scheu C and Bein T 2014 Tin doping speeds up hole transfer during light-driven water oxidation at hematite photoanodes *Phys. Chem. Chem. Phys.* **16** 24610–20
[29] Kondofersky I, Dunn H K, Müller A, Mandlmeier B, Feckl J M, Fattakhova-Rohlfing D, Scheu C, Peter L M and Bein T 2015 Electron collection in host-guest nanostructured hematite photoanodes for water splitting: the influence of scaffold doping density *ACS Appl. Mater. Interfaces* **7** 4623–30

[30] Riha S C, Devries Vermeer M J, Pellin M J, Hupp J T and Martinson A B F 2013 Hematite-based photo-oxidation of water using transparent distributed current collectors *ACS Appl. Mater. Interfaces* **5** 360–7

[31] Sun Y, Chemelewski W D, Berglund S P, Li C, He H, Shi G and Mullins C B 2014 Antimony-doped tin oxide nanorods as a transparent conducting electrode for enhancing photoelectrochemical oxidation of water by hematite *ACS Appl. Mater. Interfaces* **6** 5494–9

[32] Wang L, Palacios-Padrós A, Kirchgeorg R, Tighineanu A and Schmuki P 2014 Enhanced photoelectrochemical water splitting efficiency of a hematite-ordered Sb:SnO$_2$ host-guest system *ChemSusChem* **7** 421–4

[33] Tsui K, Zhang Y, Yang S and Fan Z 2014 Efficient photoelectrochemical water splitting with ultrathin films of hematite on three-dimensional nanophotonic structures *Nano Lett.* **14** 2123–9

[34] Mandlmeier B, Minar N K, Feckl J M, Fattakhova-Rohlfing D and Bein T 2014 Tuning the crystallinity parameters in macroporous titania films *J. Mater. Chem.* A **2** 6504

[35] Liu Y, Peters K, Mandlmeier B, Müller A, Fominykh K, Rathousky J, Scheu C and Fattakhova-Rohlfing D 2014 Macroporous indium tin oxide electrode layers as conducting substrates for immobilization of bulky electroactive guests *Electrochim. Acta* **140** 108–15

[36] Strecker A, Salzberger U and Mayer J 1993 Specimen preparation for transmission electron microscopy: reliable method for cross-sections and brittle materials *Prakt. Metallogr.* **30** 482–95

[37] Klahr B M, Martinson A B F and Hamann T W 2011 Photoelectrochemical investigation of ultrathin film iron oxide solar cells prepared by atomic layer deposition *Langmuir* **27** 461–8

[38] Maslen E N, Streltsov V A, Streltsova N R and Ishizawa N 1994 Synchrotron x-ray study of the electron density in a-Fe$_2$O$_3$ *Acta Crystallogr.* B **50** 435–41

[39] Tanisaki S 1960 Crystal structure of monoclinic tungsten trioxide at room temperature *J. Phys. Soc. Japan* **15** 573–81

[40] Hisatomi T, Le Formal F, Cornuz M, Brillet J, Tétreault N, Sivula K and Grätzel M 2011 Cathodic shift in onset potential of solar oxygen evolution on hematite by 13-group oxide overlayers *Energy Environ. Sci.* **4** 2512

[41] Tilley S D, Cornuz M, Sivula K and Grätzel M 2010 Light-induced water splitting with hematite : improved nanostructure and iridium oxide catalysis *Angew. Chem., Int. Ed. Engl.* **122** 6549–52

[42] Zhong D K, Sun J, Inumaru H and Gamelin D R 2009 Solar water oxidation by composite catalyst/r-Fe$_2$O$_3$ photoanodes *J. Am. Chem. Soc.* **131** 6086–7

[43] Peter L M, Wijayantha K G U and Tahir A A 2012 Kinetics of light-driven oxygen evolution at $\alpha$-Fe$_2$O$_3$ electrodes *Faraday Discuss.* **155** 309–22